Rapid and Precise Molecular Nanofiltration Using Ultra-Thin-Film Membranes Derived from 6,6′-Dihydroxy-2,2′-biphenyldiamine

Rapid and Precise Molecular Nanofiltration Using Ultra-Thin-Film Membranes Derived from 6,6'-Dihydroxy-2,2'-biphenyldiamine

Youcai Chen[+], Wenxiong Shi[+], Shao-Lu Li, Mengfan Wang, Jian Wang, Shuang Hao, Genghao Gong, Chunchun Ye,* Neil B. McKeown and Yunxia Hu**

[+] These authors contributed equally to this work.

Y. Chen,[+] S.-L. Li, M. Wang, S. Hao, G. Gong, Y. Hu
State Key Laboratory of Separation Membranes and Membrane Processes
School of Materials Science and Engineering
Tiangong University
Tianjin 300387, P.R. China
E-mail: lishaolu@tiangong.edu.cn, yunxiahu@tiangong.edu.cn

W. Shi[+]
Institute for New Energy Materials and Low Carbon Technologies,
School of Materials Science and Engineering,
Tianjin University of Technology,
Tianjin 300384, P.R. China.

C. Ye, N. B. McKeown
EaStCHEM
School of Chemistry,
University of Edinburgh,
Scotland EH9 3FJ, UK.
E-mail: chunchun.ye@ed.ac.uk

J. Wang
The Institute of Seawater Desalination and Multipurpose Utilization, MNR (Tianjin),
Tianjin 300192, P.R. China

Keywords: Interfacial Polymerization · 6,6'-Dihydroxy-2,2'-biphenyldiamine Monomer · Selective Cross-linking · Organic Solvent Nanofiltration · Molecular Separation

Abstract

A key challenge in efficient molecular separation is fabricating large-scale, highly selective polymeric membranes with precise pore control at the molecular scale. Herein, we introduce a new contorted monomer 6,6'-dihydroxy-2,2'-biphenyldiamine (DHBIPDA) as a building block to generate cross-linked, ultra-thin microporous nanofilms (sub-10 nm) via interfacial polymerization, enabling rapid and precise molecular nanofiltration. Using trimesoyl chloride (TMC) as the cross-linker instead of diacyl chloride (TPC) significantly reduces the pore sizes within the membranes and achieves a narrower pore distribution due to a semi-crystalline structure. The film structures are confirmed using comprehensive characterization techniques including wide-angle X-ray scattering (WAXS), X-ray diffraction (XRD), positron annihilation lifetime spectroscopy (PALS), CO_2 adsorption analysis, and molecular-scale simulation. The DHBIPDA/TPC and DHBIPDA/TMC membranes achieve methanol permeance values of up to 16.4 LMH bar^{-1} and 15.1 LMH bar^{-1} coupled with molecular weight cutoffs (MWCOs) as low as 283 Da and 306 Da, respectively, outperforming most high-performance polymeric membranes. The DHBIPDA/TPC membrane demonstrates both higher permeance and higher selectivity compared to its relatively disordered counterpart DHBIPDA/TMC, consistent with characterisation data. The DHBIPDA-derived membrane efficiently separates dye mixtures with similar molecular weights and enables effective recycling of organometallic homogeneous catalysts, suggesting its potential for industrial applications.

1. Introduction

Organic solvent nanofiltration (OSN) is emerging as an efficient membrane separation technology due to its low energy consumption, high efficiency and environmental friendliness compared to conventional heat-related separation techniques. OSN hold significant promise for molecular fractionation and purification of organic liquids, making it highly relevant for applications in the fine chemical, petroleum and pharmaceutical industries, including small-molecule separation, crude oil separation, and recovery of solvents and homogeneous catalysts *etc.*[1] However, the widespread adoption of OSN processes is hindered by ubiquitous and pernicious trade-off between membrane permeability and selectivity. To address this challenge, there is a critical need to design sophisticated membranes that can be fabricated on a scalable basis to promote fast and nanoscale molecular separation.[2]

Thin-film composite (TFC) reverse osmosis and nanofiltration membranes, manufactured using the interfacial polymerization (IP) strategy, dominate the current membrane sales market for water treatment.[3] These membranes feature in-situ generated highly cross-linked polymer networks that exhibit demonstrated stability in various organic solvents.[4] However, membranes derived from conventional monomeric materials often lack sufficient porosity and show limited solvent permeance when applied in OSN applications. Microporous materials with abundant interconnected microcavities smaller than 2 nm offer a promising solution, providing membranes with exceptional solvent permeance and high solute retention.[5] Despite the potential benefits, manufacturing defects-free membranes from crystalline microporous materials (*e.g.*, zeolites, covalent organic frameworks (COFs) and metal organic frameworks (MOFs)) remains technically challenging and time-consuming, especially on a large scale.[6] Consequently, there is a shift towards designing and fabricating amorphous polymer membranes with high-density microporous structures resembling their crystalline counterparts to advance OSN membrane technology.[7]

Recent advancements including using macrocyclic molecules with intrinsic cavities, such as cyclodextrins (CD),[8] trianglamine,[9] double cyclic Noria,[10]

pillar[n]arenes[11] and 3D porous organic cages[12], as sole aqueous monomeric components via IP with acyl chloride to produce high-performance OSN membranes. This approach capitalizes on permeant cavities that translate into interconnected membrane pores. Another intriguing approach involves using rigid and contorted new reactive monomers inspired by the concept of polymers of intrinsic microporosity (PIMs) [13] to create ultra-thin cross-linked PIM layers *in situ* through straightforward IP methods.[14] For example, triptycene-based tetraacyl chloride (Trip),[5a] PIM-motif monomers like 5,5′,6,6′-tetrahydroxy-3,3,3′,3′-tetramethylspirobisindane (TTSBI) and 9,9-bis(4-hydroxyphenyl)fluorene (BHPF),[5b] bulky adamantane diamine[15] and 2,2′-biphenol derivatives[16] have all contributed to create selective layers with high density of microvoid elements, affording fast and selective nanofiltration. Despite these improvements, the uniformity of pore size and pore interconnectivity remains critical for effective molecular sieving.[17] For example, ultra-thin CD nanofilms with well-aligned pores are achieved by crossing amino-CD with diacyl chloride (TPC), but not trimesoyl chloride (TMC).[7b, 18] When altering the oil phase monomer from TMC to diacyl chloride TPC (terephthaloyl chloride) or IPC (isophthaloyl dichloride), the selectivity of the bisphenol-derived OSN membrane decreased, with an increase in molecular weight cut-off (MWCO) to 300 Da and 373 Da, respectively, while maintaining higher methanol permeance.[19] Therefore, special attention must be given to selective cross-linking and the precise tuning of microvoid uniformity and interconnectivity in developing novel monomeric molecules.

In this work, we designed and synthesized a novel biphenyl derivative, 6,6′-dihydroxy-2,2′-biphenyldiamine (DHBIPDA), with enhanced steric hindrance and/or reactive amine groups compared to our previous biphenol (BIPOL) analogues,[16] incorporating altered geometry of reactive groups (Figure 1). By employing this contorted monomer DHBIPDA in reactions with TMC or diacyl chloride TPC via IP method, we successfully fabricated molecularly microporous ultrathin polyesteramide nanofilms. We observed that the DHBIPDA nanofilm constructed from diacyl chloride showed partially crystalline feature with a more ordered microstructure and smaller

pore size compared to that from TMC. This was supported by various analytical techniques including WAXS, XRD, PALS, CO_2 physical adsorption experiments and molecular simulation. As a result of this structural refinement, the corresponding composite membrane demonstrated higher selectivity and superior solvent permeance in OSN. Notably, Our DHBIPDA membrane effectively separated dye mixtures with similar molecular weights and enabled the recycling of organometallic homogeneous catalysts used in asymmetric hydrogenation reactions while allowing small reactants and products to pass through freely, which highlights the industrial utilization potentials.

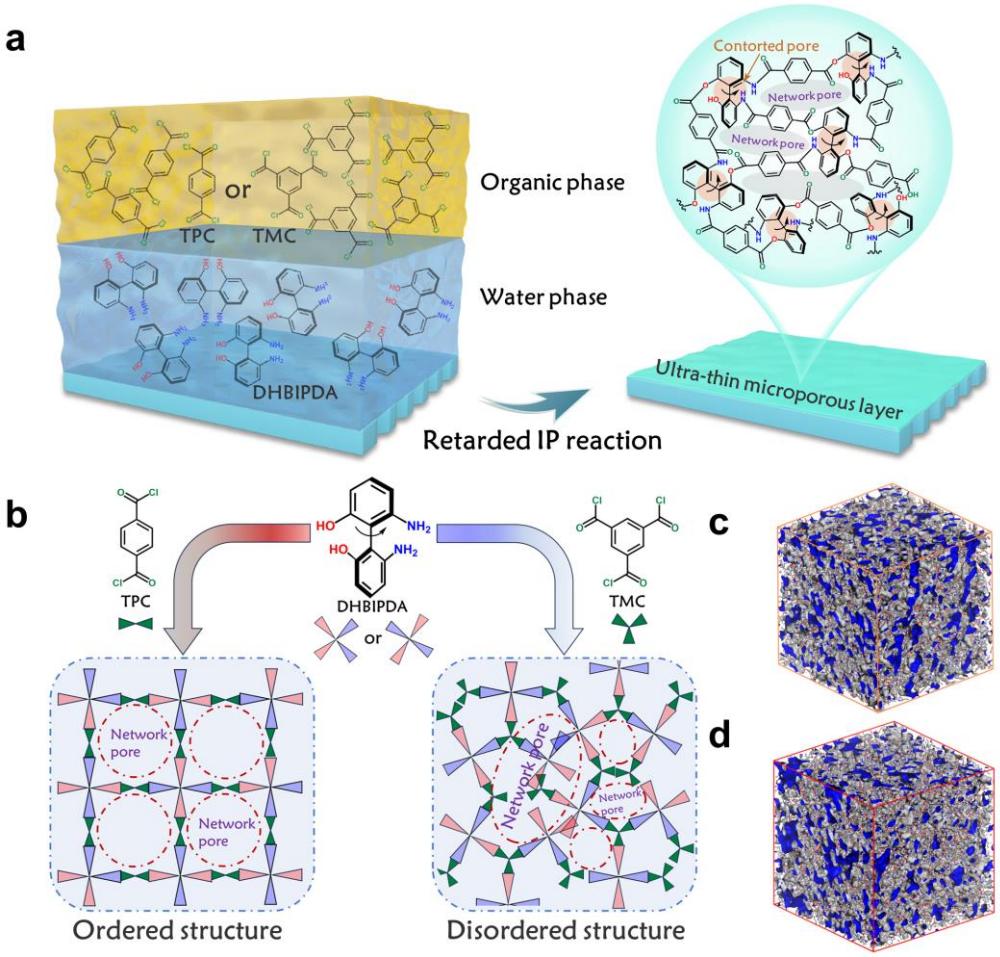

Figure 1. Synthesis of polyesteramide nanofilms. (a) Schematic illustration of the interfacial polymerization (IP) reaction to create microporous polyesteramide nanofilms between DHBIPDA in the aqueous solution and TMC/TPC in the oil phase, resulting in crosslinked rigid-twistable microporous polymer networks (right). (b) Microstructure diagram of the DHBIPDA-derived nanofilms. Three-dimensional views of amorphous models containing (c) DHBIPDA/TPC and (d) DHBIPDA/TMC polyesteramide networks, visualized using Materials Studio. Blue color: surface at probe radius of 1 Å diameter; Gray color: accessible porous surface. Cell size: 80 Å×80 Å×80 Å.

2. Results and Discussion

2.1. Ultrathin Nanofilms Fabrication by IP

The monomer DHBIPDA was facilely synthesized starting from 2-bromo-1-methoxy-3-nitrobenzene in three steps. First, a Cu-catalyzed Ullmann-coupling reaction was performed, followed by hydrogenation of the nitro groups, and finally demethylation to afford the desired product. Detailed synthetic procedures and characterizations are provided in the Supporting Information. As depicted in Figure 1a, DHBIPDA features two amino and two phenolic hydroxyl reactive sites at 2,2'- and 6,6'-position of a biphenyl motif, enabling it to undergo IP reaction with acyl chloride. The unique molecular structure and steric hindrance results in a non-planar configuration of the biphenyl rings, especially evident after cross-linking, thus facilitating the formation of nanofilms with exceptionally high fractional free volume. Molecular dynamic simulation (MD) results (Figure 1c-d) demonstrated the highly microporous texture of the resulting polyesteramide nanofilms. Photographs in Figure 2a-c depict self-standing nanofilms synthesized at the oil-water interface, showcasing their ability to float on the water surface and be supported by a wire loop without visible cracks, indicating their mechanical robustness. SEM images (Figure 2d) of interfacially prepared polymer solids reveals a film-like morphology. Additionally, Figure 2e-f shows a free-standing nanofilm transferred onto porous AAO substrate after a 5-min reaction, indicating its defect-free and ultra-thin feature (around 20 nm).

SEM images of DHBIPDA composite membranes on a PAN substrate exhibit continuous and smooth surface morphology. However, the thickness of the top polyesteramide layer is difficult to discern in cross-sectional images due to its ultra-thin nature (<20 nm) (Figure 2g and Figures S6-10).[5b, 7b] Based on our previous 2,2'-bisphenol work,[16] we have observed a strict correlation between the thickness of free-standing nanofilms and composite membranes due to the retarded IP reaction. Therefore, we turned to quantify the thickness of the free-standing nanofilms synthesized under analogous parameters. We first conducted AFM analysis of nanofilms deposited on a silica wafer. As shown in Figure 2h-k and Figures S11-12, film thickness increases with

increasing IP reaction time from 30 s to 5 min, ranging from approximately 7 nm to 20 nm for DHBIPDA/TMC and 10 nm to 19 nm for DHBIPDA/TPC nanofilms, respectively. Spectroscopic ellipsometry (SE) results (Figure 2l) are consistent with AFM observation, showing film thicknesses of around 10 nm and 13 nm for DHBIPDA/TMC and DHBIPDA/TPC films after a 1-min IP reaction. In contrast, the film thickness of amino-BIPOL/TMC is around 5 nm,[16] indicating distinct film forming process during IP despite their similar molecular structure. Notably, the thickness of DHBIPDA/TPC film shows a slow increasing trend, plateauing after a 2-min duration, suggesting an ultra-small aperture size that prevents further penetration of monomeric DHBIPDA molecules upward.[20]

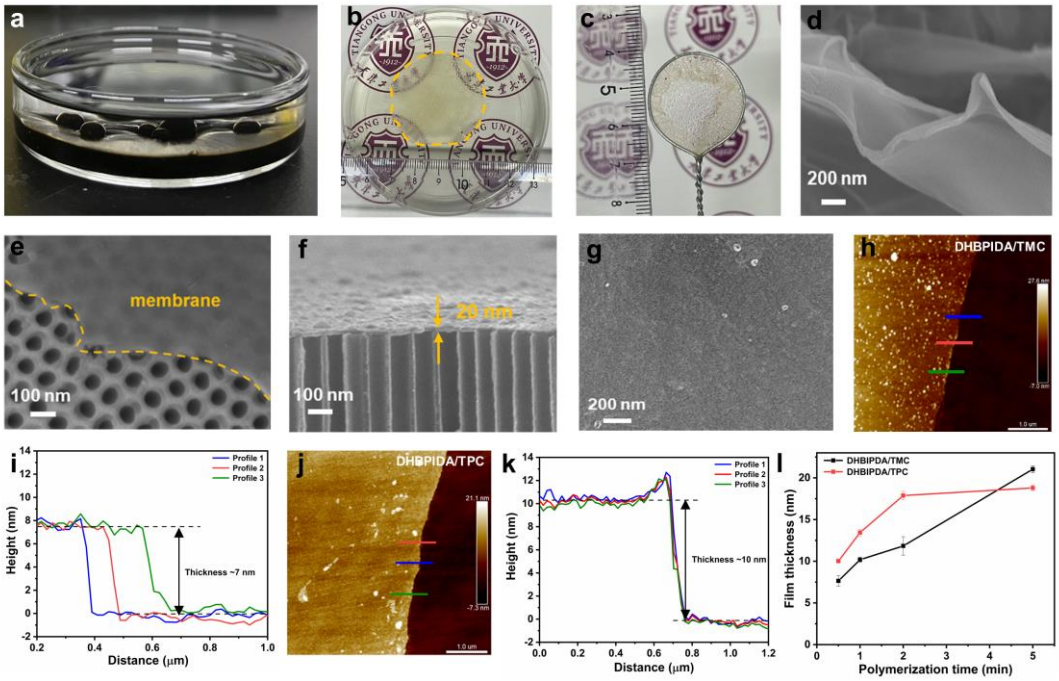

Figure 2. Morphology characterization of polyesteramide nanofilms prepared by interfacial polymerization. (a-c) Optical photographs of the freestanding DHBIPDA/TMC nanofilm formed at the water-oil interface, transferred on the surface of the water and captured by a wire loop. (d) SEM image of freestanding DHBIPDA/TMC polymer powder fabricated by rigorous mixing of a solution of TMC in Isopar G and a solution of DHBIPDA in water. The as-fabricated DHBIPDA/TMC nanofilm (IP 5 min) were transferred onto the AAO substrate of the (e) top-view and (f) cross-sectional SEM images. (g) SEM image of top surface of the DHBIPDA/TMC composite membrane. AFM height images and corresponding height profiles of nanofilms (IP 30 s) prepared by TMC (h, i), TPC (j,k) and DHBIPDA transferred on silicon wafers. (i) Thickness plots of nanofilms prepared with different IP reaction time measured by spectroscopic ellipsometry (SE).

2.2. Membrane Structure Characterization and Simulation

The membrane surface chemical structure was investigated by FT-IR spectra and XPS analysis, as presented in Figure 3a-d and Figures S15 and 16. After polymerization, new IR peaks appeared at 1740 cm^{-1}, 1626 cm^{-1} and 1548 cm^{-1}, associated with the stretching bands of -C=O bonds and N-H vibration in the formed ester and amide groups. In XPS analysis, the DHBIPDA composite membranes showed a significant decrease in N element content upon covering with the polyesteramide layer compared to the bare PAN substrate. The deconvolution narrow scan spectrum also confirmed the expected chemical structure of the membranes. These results demonstrated the successful formation of the polyesteramide film via IP reaction between DHBIPDA and TMC/TPC. In addition, TGA results demonstrated that DHBIPDA nanofilms are stable up to 280 °C in a nitrogen atmosphere (Figure 3e). The surface charge of the DHBIPDA membranes was examined by streaming potential test, revealing an amphoteric character with charges of approximately -30 mV/-24 mV at pH 7 for the DHBIPDA/TMC and DHBIPDA/TPC membranes, respectively. Membrane derived from triacyl chloride TMC exhibited a significantly more negative charge compared to these prepared from diacyl chloride TPC (Figure 2f).

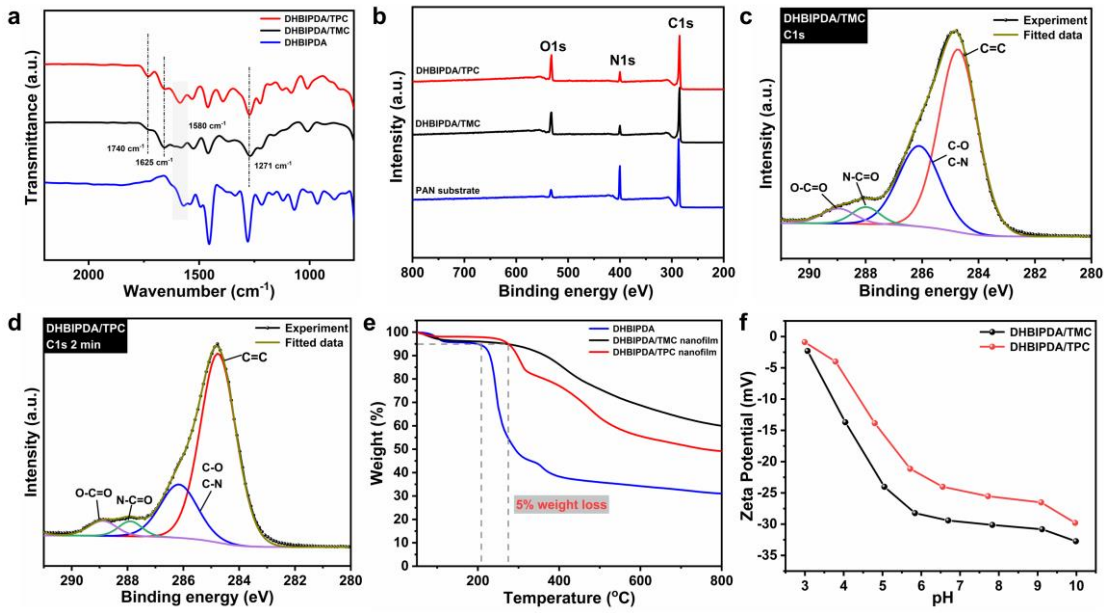

Figure 3. Chemical structure characterizations. (a) FT-IR spectra of DHBIPDA monomer and the resulting film powders. (b) X-ray photoelectron spectroscopy (XPS) survey spectrum of the PAN substrate, DHBIPDA composite membranes. XPS C1s spectra of (c) DHBIPDA/TMC and (d)

DHBIPDA/TPC composite membranes. (e) Thermogravimetric analysis (TGA) profiles of DHBIPDA monomer and the resulting polyesteramide film powders. (f) Surface zeta potential curves of the DHBIPDA composite membranes.

Wide-angle X-ray scattering (WAXS) analysis (Figure 4a-c) was employed to probe microstructure of the two polyesteramide polymer film. Compared to the DHBIPDA/TMC membrane, the DHBIPDA/TPC membrane exhibited more distinct Debye-Scherrer rings in the 2D WAXS pattern, indicating preferential orientation and a semi-crystalline structure in the layer derived from diacyl chloride TPC.[4b, 18] Sharp and intense peaks appeared at 1.24, 1.78, and 1.98 $Å^{-1}$ in the extracted 1D X-ray scatting profile of the TPC membrane corresponded to ordered crystal parts with lamella distances of 5.06, 3.53, and 3.17 Å, likely due to the configuration flexibility of the rotatable DHBIPDA with multiple crosslinking sites. In contrast, the DHBIPDA/TMC film exhibited broad peaks, indicating its amorphous nature. X-ray diffraction (XRD) spectra (Figure 4d) confirmed the WAXS results with sharp diffraction peaks only observed in the DHBIPDA/TPC membrane, suggesting the presence of ordered crystal structure compared to DHBIPDA/TMC membrane.

The microporous characteristics of DHBIPDA polymer powders were further confirmed by CO_2 adsorption isotherms, showing steep uptake at relatively low pressures and giving specific surface area of 156.8 and 120.3 $m^2 g^{-1}$ for film derived from TPC and TMC, respectively (Figure 4e). The enhanced microporosity is attributed to the sterically contorted and multifunctional sites for cross-linking of the monomer DHBIPDA. The TPC film exhibited a larger fraction of ultramicropores (<7 Å) and submicropores (<4 Å), along with a lower fraction of larger micropores (>7 Å) compared to the material derived from TMC as shown in the inserted pore size distribution curves. Positron annihilation lifetime spectroscopy (PALS) [12b, 21] further revealed variations in free volume between the two films. The DHBIPDA/TPC film exhibited an average cavity radius centering at ~1.75 Å, while the DHBIPDA/TMC film had a larger size of ~1.89 Å. Additionally, the TPC film showed a narrower pore size distribution compared to the TMC film (Figure 4f). These align with the results calculated from MWCOs data using neutral small molecules as solutes in aqueous

solution (Figures S19 and 20), indicating that the microstructure variations in the DHBIPDA films are attributed to selective cross-linking by bifunctional TPC rather than the trifunctional TMC, resulting in a more ordered film structure.

Microstructure of the two DHBIPDA films were further visualized based on the realistic structural models generated by molecular simulation. The simulation details are provided in the Supporting methods and the results are shown in Figure 4g-i and Figures S21-23. Large fractions of highly interconnected voids were observed, particularly with probe radius less than 0.80 Å, indicating high microporosity and cavity interconnectivity for easy transport of small molecules. The simulation results also showed that the DHBIPDA/TMC film possessed larger micropores with radius of 0.3 to 0.45 nm compared to the TPC membrane, consistent with BET and PALS analysis results. These microstructural characterizations of the two DHBIPDA films contribute to an understanding of their variations in OSN separation performances detailed in the following section.

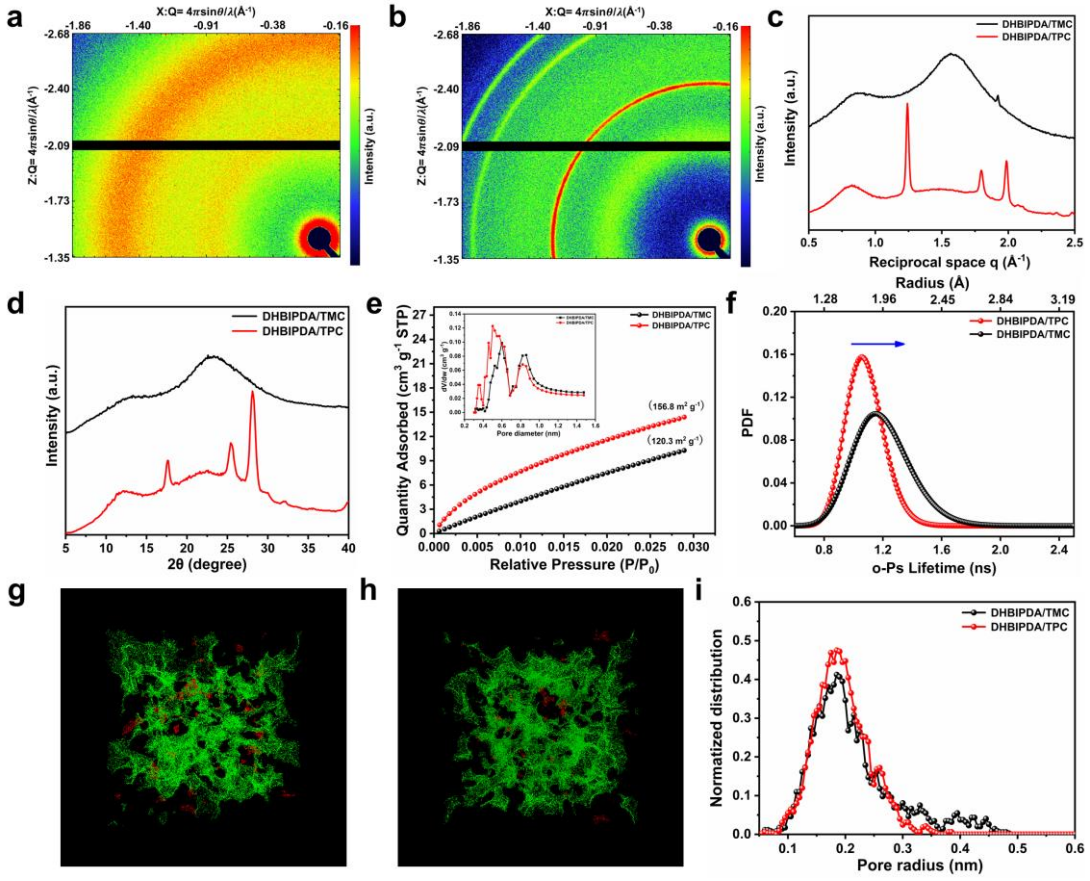

Figure 4. Characterizations of the microporous structure of the DHBIPDA polyesteramide nanofilms. (a, b) WAXS 2D scattering patterns of two nanofilms. (c) WAXS one-dimensional images of the two polyesteramide nanofilms. (d) XRD pattern of the two polyesteramide nanofilms. (e) CO_2 adsorption isotherms measured at 273 K for DHBIPDA polymer powders. The inset indicates the related pore size distributions according to CO_2 adsorption isotherms using nonlocal density functional theory (NLDFT). (f) o-Ps lifetime and free volume properties of the membranes were characterized in the range of positron incident energy from 0.18 to 30 KeV. Molecular simulation, snapshots of free volume measured with probes of 0.70 Å radius for membrane models of (g) DHBIPDA/TMC and (h) DHBIPDA/TPC; Green color: interconnected voids; Red color: disconnected voids. (i) Simulation results of pore size distribution of prepared two DHBIPDA membranes.

2.3. OSN Separation Performance

The ultra-thin film thickness and highly microporous features of the DHBIPDA membranes are anticipated to enable them ultra-high solvent permeance while maintaining controllable solutes selectivity. Thus, we conducted a detailed evaluation of the separation performance of the prepared DHBIPDA composite membranes at 25°C. As shown in Figure 5a, the methanol permeance of the as-prepared membranes present a gradual decrease with the extension of the IP reaction time from 30 s to 5 min, which correlates well with the increasing film thickness trend observed at longer reaction times (Figure 2i). For DHBIPDA/TPC and DHBIPDA/TMC membrane with an IP reaction time of 30 s, the methanol permeance reached as high as 16.4 LMH bar^{-1} and 15.1 LMH bar^{-1}, respectively. This ultra-high solvent permeance can be attributed to their microporous structure and high pore interconnectivity. Notably, Membrane solute rejection is not significantly dependent on the IP duration, implying that defect-free DHBIPDA nanofilms are generated even at a short IP time of 30 s (Figures S25 and 26). That can be associated with the rigid skeleton and short linker distance of the multiple reactive sites of monomer DHBIPDA, resulting in a highly cross-linked network structure of the separating layer.

Figure 5b shows the dye rejection results of the two DHBIPDA composite membranes prepared with an IP reaction of 30 s. These membranes exhibited good retaining capacities for most dye molecules in methanol, particularly those with M.W. exceeding 320 Da. The MWCOs are notably low, at 283 Da for DHBIPDA/TPC

membrane and 306 Da for DHBIPDA/TMC membrane. Similarly, evaluation of aqueous solution MWCOs for the two DHBIPDA composite membranes by filtering neutral small molecules yielded values of 233 Da for DHBIPDA/TPC membrane and 256 Da for DHBIPDA/TMC membrane (Figures S19 and S20). The relatively smaller MWCOs in aqueous media may be attributed to the film swelling effect in methanol and/or solute hydration effect in aqueous solution, phenomena observed in other OSN membranes.[8a, 16] Notably, despite the DHBIPDA/TPC membrane exhibiting less negative charge, it shows significantly higher solute selectivity across the entire range compared to the membrane using the oil cross-linker TMC. This performance variation aligns with film pore structure characterizations and simulation results, with the DHBIPDA/TMC film showing more disordered structure and possessing large micropores that allow passage of larger solutes.

Figure 5c and Figure S29 demonstrate that solvent permeance of the two DHBIPDA membrane correlates linearly with combined parameters (*i.e.*, molecular volume, viscosity, and solubility parameter), except for acetone and water. DHBIPDA/TPC membrane exhibited the highest permeance with acetone of 36.2 LMH bar^{-1}, attributed to its low viscosity and suitable polarity comparable with the DHBIPDA film materials. This membrane shows relatively low permeance with water of 3.9 LMH bar^{-1} due to its high viscosity and high polarity. These results indicated that the film microstructure, material, and solvent parameters collectively influence permeance. Long-term operation stability of the two DHBIPDA membranes was tested through an 80 h continuous filtration experiments using Orange G (OG) methanol solution, followed by sequential switching of pure solvent (methanol, THF, ethanol, toluene, water and methanol again) within 70 h (Figures S31-34). In addition, the DHBIPDA composite membranes exhibited high rejection for divalent-anions salts Na_2SO_4, *i.e.*, 96.3% for DHBIPDA/TPC membrane and 97.1% for DHBIPDA/TMC membrane (Figures S37 and 38). For monovalent-anions salts NaCl, the DHBIPDA/TPC membrane showed a higher rejection with value of 62.3% compared

to DHBIPDA/TMC membrane (36.5%), attributed to smaller aperture size of DHBIPDA/TPC.

A comparison of separation performance between DHBIPDA membranes in methanol and recently reported OSN membranes is presented in Figure 5d and Table S5. The perm-selectivity of the DHBIPDA membrane proves superior to most high-permeance OSN membranes, especially with high rejection rates towards small organic solutes with M.W. around 300 Da. Notably, DHBIPDA/TPC membrane achieved a MWCO as low as 283 Da with high methanol permeance of 16.4 LMH bar^{-1}, even slightly outperforming our previous reported bisphenol OSN membrane.[16] The activated PA on AAO film shows a prominent OSN membrane while its fabrication involves multi-step elaborate processing that keeps these films at the lab scale. In contrast, the ease of processing combined with comparable high performance endow BIPDA membranes with more industrial-scale potential.

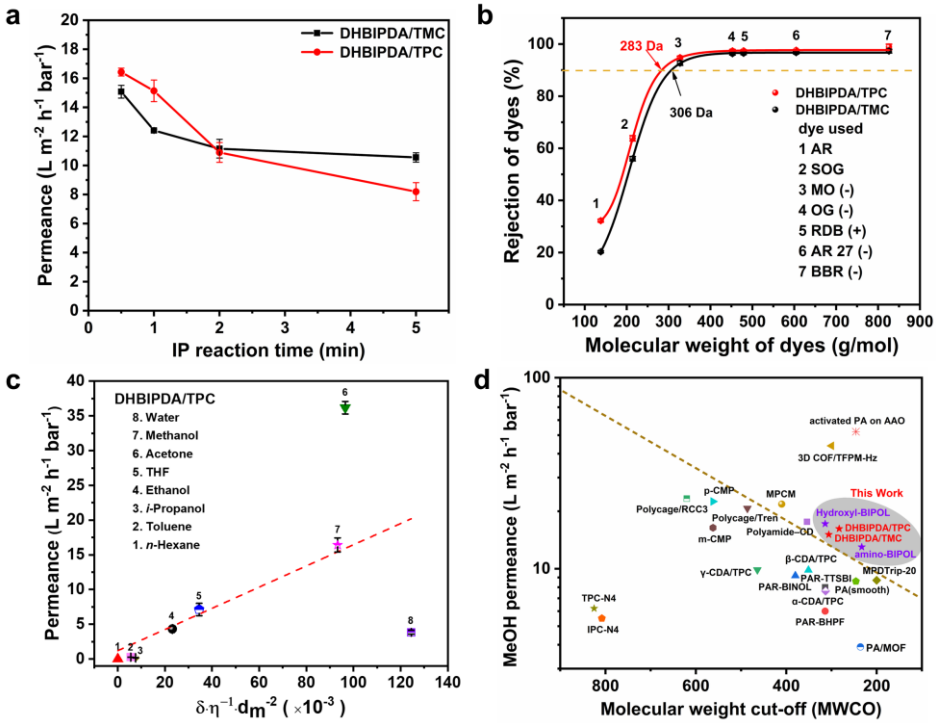

Figure 5. Separation performance of the DHBIPDA composite membranes. (a) Methanol permeance of the DHBIPDA membranes fabricated with different IP reaction times. (b) Rejection of dyes in solvent methanol with different molecular weights through the DHBIPDA composite membranes prepared with IP reaction time of 30 s. (c) Solvent permeance of the DHBIPDA/TPC composite membrane versus combined solvent properties with IP reaction time of 30 s. (d) Perm-selectivity comparison of the two DHBIPDA membranes with previously reported OSN membranes in literature.

Molecular sieving capability is important for the industrial applications of OSN membranes. Therefore, we conducted the separation of mixed dyes solution containing Nile red (NR, neutral, 318 Da) and Methyl orange (MO, negative, 327 Da) using the DHBIPDA/TPC membrane. As shown in Figure S39, the filtrate appeared red, indicating the presence of NR only, which was confirmed through UV-Vis spectra. This is attributed to the near-complete rejection of the negatively charged dye MO, while allowing the neutral NR to pass through. The effective molecular sieving results from both the electrostatic force of the negatively charged membrane surface and the narrow micropore distribution of the DHBIPDA-based active layer (Figures 3f and 4).

We conducted further evaluation of the DHBIPDA membrane for the continuous recycling of a homogeneous organometallic catalyst used in chemical and pharmaceutical industries. Recovering such expensive catalysts from the product solution by conventional methods is typically challenging and labor-intensive. However, this issue can be efficiently addressed using a continuous hybrid process with the assistance of OSN separation.[1c, 22] Nevertheless, most available OSN membranes exhibit low efficiency as they generally offer low solvent permeance and/or fail to retain the large catalyst while also rejecting certain amount of products. Herein, we chose the dimethyl itaconate (DMI) asymmetric hydrogenation reaction system for demonstration (Figure 6a). As shown in Figure 6b-d, DHBIPDA membrane rejected almost all of the catalyst BINAP-Ru complex (>99%) while preserving its chemical structure. Simultaneously, it allowed the small neutral reactant DMI and product to pass through freely with low rejection rates (< 2%). A filtration experiment using a feed solution of BINAP-Ru complex in methanol over 88 h showed that the methanol permeance remained constant at ~12 LMH bar^{-1} with a >99% rejection rate, indicating effective catalyst recovery (Figure 6e). Therefore, our DHBIPDA-based membrane presents significant potential for homogeneous catalyst recycling compared to conventional technologies such as extraction and chromatography.[23]

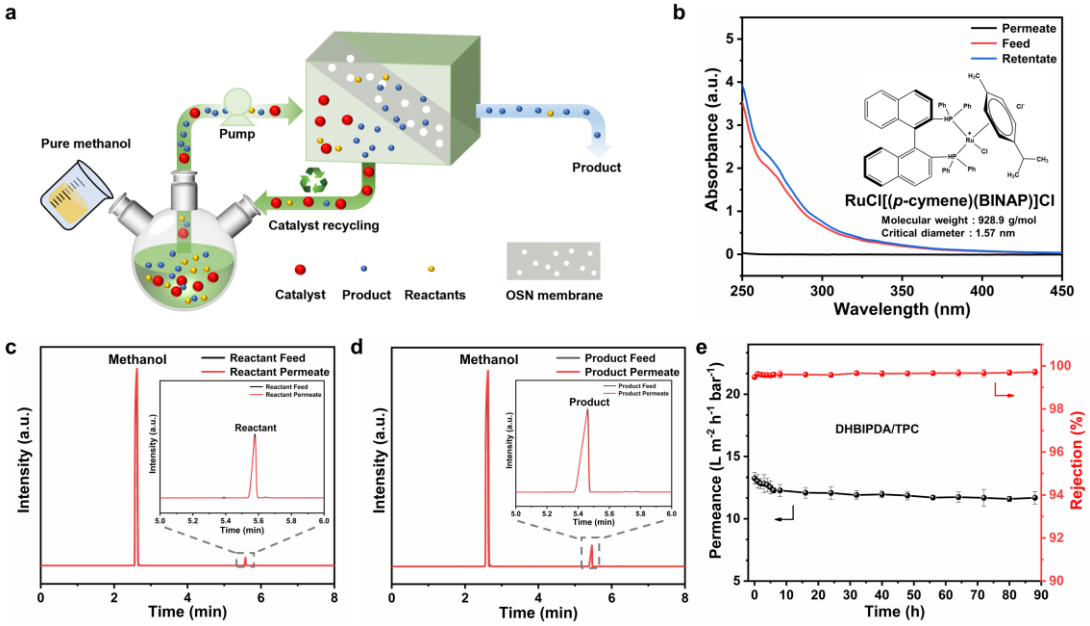

Figure 6. Recovery of homogeneous catalysts using DHBIPDA composite membrane. (a) Schematic diagram of OSN-assisted continuous BINAP-Ru (II) catalyst recovery process. The process was operated in a continuous dead-end system with a trans-membrane pressure of 5 bar. (b) UV–Vis absorption spectra of a methanol solution of BINAP-Ru (II) complex in the feed and permeate filtering of DHBIPDA/TPC composite membrane, the inset shows the chemical structure of BINAP-Ru (II) complex. Gas Chromatograph (GC) was utilized to analyze the concentration of feed and filtrate after filtration through and DHBIPDA/TPC membrane for (c) reactant and (d) product. (e) Long-term filtration experiment using the methanol solutions of BINAP-Ru (II) complex for DHBIPDA/TPC composite membrane.

3. Conclusion

In this study, we developed high-performance microporous TFC membranes for OSN process using a novel mutifunctional derivative of BIPDA via interfacial polymerization. We discovered that employing the oil-phase cross-linker diacyl chloride TPC led to selective cross-linking and a more ordered film structure compared to triacyl chloride TMC. This improvement is attributed to the unique rotatable biphenyl skeleton and the spatial configuration of reactive sites with high steric hindrance. The microporous structure of the films was comprehensively characterized using techniques such as WAXS, XRD, PALS, CO_2 physical adsorption analysis and molecular simulation. The OSN performance, particularly of the DHBIPDA/TPC membrane, surpassed that of most recently reported polymeric OSN membranes, consistent with the film characterization results. Notably, the DHBIPDA membrane demonstrated

precise molecular sieving for dye mixtures with similar M.W. and enabled efficient recovery of organometallic homogeneous catalysts from reaction solutions, showcasing the potential for industrial applications.

4. Experimental Section

Composite membrane preparation: The monomer DHBIPDA was synthesized in three steps and the details are described in the Supporting Information. The DHBIPDA-based thin film composite (TFC) membranes were prepared directly on PAN UF supports by conventional interfacial polymerization method. For the membrane of DHBIPDA/TMC, the PAN substrate was first soaked in DI water overnight and then transferred onto the glass plate, it is carefully dried using dust-free paper and fixed with a PTFE frame. The aqueous phase with a pH of 11.5 containing DHBIPDA (1.0 wt%), NaOH (4.0 molar eq.) was poured onto the support and held for 2 min, and then the excess aqueous phase was removed using a rubber roller. Subsequently, the membrane was wetted by Isopar G solution containing 0.1 wt% (w/v) TMC for a certain time to form polyesteramide nanofilm. Finally, the membrane was washed with hexane and heated in an oven at 65 °C for 5 min. For the membrane of DHBIPDA/TPC, the aqueous solution consist of DHBIPDA (1.0 wt%), NaOH (4.0 molar eq.) and dodecyltrimethylammonium chloride (DTAC, 0.06 wt%), a Isopar G solution containing TPC (0.1 wt%) was used as the organic phase. The other membrane preparation steps were the same as that of DHBIPDA/TMC membranes. All membranes were fabricated at 25°C with humidity of 40 %, and all membranes were stored in DI water at 4 °C for further use.

Synthesis of freestanding nanofilms: The free-standing nanofilms were fabricated at the oil-water interface using the same IP parameters as those of TFC membranes. As shown in Figure S4, firstly, two rubber pads were stacked together and fixed on a glass plate with a clamp. Then, aqueous phase solution was carefully introduced, and organic phase solution was added slowly and kept for 30 s - 5 min. After that, the two phases were gradually extracted using a burette, resulted in the formation of the free-standing

nanofilm on a glass plate. Subsequently, the nanofilm was carefully transferred onto the water surface through rinsing with an *n*-hexane solution to eliminate residual acyl chloride monomers from the surface of the film. Upon rinsing with DI water, the nanofilm was transferred onto anodized aluminum oxide (AAO) or silicon wafer for further characterization.

Membrane separation performance evaluation: The nanofiltration tests were conducted on a lab-scale dead-end apparatus with a suspending stir bar (effective membrane area of 2.83 cm^2 in each cell, 600 rpm). The feed solution of varies dyes were setted as 50 ppm in methanol. The composite membranes were pre-compacted with pure solvent under 6 bar for at least 2 h to obtain a steady permeate flux before using. The solvent permeance (J_w, L m^{-2} h^{-1} bar^{-1}) was calculated based on the following equation:

$$J_W = V/(A \cdot \Delta t \cdot \Delta P)$$

where V represents the volume of collected permeate solution during filtration time of Δt (h), A is the effective membrane area (m^2), ΔP represents the trans-membrane pressure (bar), respectively .

The solute rejection (R, %) was calculated based on the following equation:

$$R = 1-(C_p/C_f) \times 100\%$$

where C_p and C_f are the solute concentrations of permeate and feed solutions, respectively. All experiments were carried out at 25 ± 0.5 ℃ under 5 bar, and repeated at least three times.

Supporting Information

Supporting Information is available from the Wiley Online Library or from the author.

Acknowledgements

We would like to thank the Analytical & Testing Center of Tiangong University for XPS, BET, XRD and AFM characterization. And we also appreciate the financial

support of National Natural Science Foundation of China (No. 22375145 and 22378314).

Conflict of Interest

The authors declare no conflict of interest.

References

[1] a) G. M. Shi, Y. Feng, B. Li, H. M. Tham, J.-Y. Lai, T.-S. Chung, *Prog. Polym. Sci.* **2021**, *123*, 101470; b) Y. Li, Z. Guo, S. Li, B. Van der Bruggen, *Adv. Mater. Interfaces* **2021**, *8*, 2001671; c) P. Marchetti, M. F. Jimenez Solomon, G. Szekely, A. G. Livingston, *Chem. Rev.* **2014**, *114*, 10735-10806; d) P. He, S. Zhao, C. Mao, Z. Wang, J. Wang, *CIESC Journal* **2021**, *72*, 727-747; eK. S. Goh, Y. Chen, J. Y. Chong, T. H. Bae, R. Wang, *J. Membr. Sci.* **2021**, *621*, 119008.

[2] a) Z. Wang, X. Luo, J. Zhang, F. Zhang, W. Fang, J. Jin, *Adv. Membr.* **2023**, *3*, 100063; b) S. Ali, I. A. Shah, I. Ihsanullah, X. Feng, *Chemosphere* **2022**, *308*, 136329; c) D. Yu, X. Xiao, C. Shokoohi, Y. Wang, L. Sun, Z. Juan, M. J. Kipper, J. Tang, L. Huang, G. S. Han, H. S. Jung, J. Chen, *Adv. Funct. Mater.* **2023**, *33*, 2211983.

[3] a) Z. Wang, S. Liang, Y. Kang, W. Zhao, Y. Xia, J. Yang, H. Wang, X. Zhang, *Prog. Polym. Sci.* **2021**, *122*, 101450; b) X. Lu, M. Elimelech, *Chem. Soc. Rev.* **2021**, *50*, 6290-6307.

[4] a) Y. Li, S. Li, J. Zhu, A. Volodine, B. Van der Bruggen, *Chem. Sci.* **2020**, *11*, 4263-4271; b) A. Yao, J. Du, Q. Sun, L. Liu, Z. Song, W. He, J. Liu, *ACS Nano* **2023**, *17*, 22916–22927.

[5] a) Z. Ali, B. S. Ghanem, Y. Wang, F. Pacheco, W. Ogieglo, H. Vovusha, G. Genduso, U. Schwingenschlögl, Y. Han, I. Pinnau, *Adv. Mater.* **2020**, *32*, 2001132; b) M. F. Jimenez-Solomon, Q. Song, K. E. Jelfs, M. Munoz-Ibanez, A. G. Livingston, *Nat. Mater.* **2016**, *15*, 760-767; c) X. Shi, Z. Zhang, C. Yin, X. Zhang, J. Long, Z. Zhang, Y. Wang, *Angew. Chem., Int. Ed.* **2022**, *61*, e202207559; d) Y. Zhang, J. Guo, G. Han, Y. Bai, Q. Ge, J. Ma, C. H. Lau, L. Shao, *Sci. Adv.* **2021**, *7*, eabe8706.

[6] a) S. Li, R. Dong, V.-E. Musteata, J. Kim, N. D. Rangnekar, J. R. Johnson, B. D. Marshall, S. Chisca, J. Xu, S. Hoy, B. A. McCool, S. P. Nunes, Z. Jiang, A. G. Livingston, *Science* **2022**, *377*, 1555-1561; b) S. Chisca, V.-E. Musteata, W. Zhang, S. Vasylevskyi, G. Falca, E. Abou-Hamad, A.-H. Emwas, M. Altunkaya, S. P. Nunes, *Science* **2022**, *376*, 1105-1110.

[7] a) C. Liu, J. Yang, B.-B. Guo, S. Agarwal, A. Greiner, Z.-K. Xu, *Angew. Chem., Int. Ed.* **2021**, *60*, 14636-14643; b) T. Huang, T. Puspasari, S. P. Nunes, K.-V. Peinemann, *Adv. Funct. Mater.* **2020**, *30*, 1906797; c) H. Guo, F. Li, X. Shui, J. Wang, C. Fang, L. Zhu, *ACS Appl. Mater. Interfaces* **2023**, *15*, 37077–37085.

[8] a) J. Liu, D. Hua, Y. Zhang, S. Japip, T.-S. Chung, *Adv. Mater.* **2018**, *30*, 1705933; b) L. F. Villalobos, T. Huang, K.-V. Peinemann, *Adv. Mater.* **2017**, *29*, 1606641.

[9] T. Huang, B. A. Moosa, P. Hoang, J. Liu, S. Chisca, G. Zhang, M. AlYami, N. M. Khashab, S. P. Nunes, *Nat. Commun.* **2020**, *11*, 5882.

[10] Z. Zhai, C. Jiang, N. Zhao, W. Dong, P. Li, H. Sun, Q. J. Niu, *J. Membr. Sci.* **2020**, *595*, 117505.

[11] W. Fu, Y. Huang, L. Deng, J. Sun, S.-L. Li, Y. Hu, *J. Membr. Sci.* **2022**, *655*, 120583.

[12] a) X. Li, W. Lin, V. Sharma, R. Gorecki, M. Ghosh, B. A. Moosa, S. Aristizabal, S. Hong, N. M. Khashab, S. P. Nunes, *Nat. Commun.* **2023**, *14*, 3112; b) S.-H. Liu, J.-H. Zhou, C. Wu, P. Zhang, X. Cao, J.-K. Sun, *Nat. Commun.* **2024**, *15*, 2478.

[13] a) N. B. McKeown, *Curr. Opin. Chem. Eng.* **2022**, *36*, 100785; b) Z.-X. Low, P. M. Budd, N. B. McKeown, D. A. Patterson, *Chem. Rev.* **2018**, *118*, 5871-5911.

[14] a) H. Peng, K. Yu, X. Liu, J. Li, X. Hu, Q. Zhao, *Nat. Commun.* **2023**, *14*, 5483; b) H. Peng, Y. Su, X. Liu, J. Li, Q. Zhao, *Adv. Funct. Mater.* **2023**, *33*, 2305815.

[15] S. Wang, Z. Wang, S. Zhu, S. Liu, F. Zhang, J. Jin, *J. Membr. Sci.* **2023**, *675*, 121540.

[16] S.-L. Li, G. Chang, Y. Huang, K. Kinooka, Y. Chen, W. Fu, G. Gong, T. Yoshioka, N. B. McKeown, Y. Hu, *Angew. Chem., Int. Ed.* **2022**, *61*, e202212816.

[17] a) Z. Zhou, D. B. Shinde, D. Guo, L. Cao, R. A. Nuaimi, Y. Zhang, L. R. Enakonda, Z. Lai, *Adv. Funct. Mater.* **2022**, *32*, 2108672; b) Z. Zhou, D. Guo, D. B. Shinde, L. Cao, Z. Li, X. Li, D. Lu, Z. Lai, *ACS Nano* **2021**, *15*, 11970–11980; c) D. Yu, L. Sun, Y. Zhang, Y. Song, C. Jia, Y. Wang, Y. Wang, M. J. Kipper, J. Tang, L. Huang, *Chem. Eng. J.* **2024**, *480*, 148009; d) Z. Zhang, X. Xiao, Y. Zhou, L. Huang, Y. Wang, Q. Rong, Z. Han, H. Qu, Z. Zhu, S. Xu, J. Tang, J. Chen, *ACS Nano* **2021**, *15*, 13178-13187; e) F. Jia, L. Yang, L. Sun, D. Yu, Y. Song, Y. Wang, M. J. Kipper, J. Tang, L. Huang, *Water Res.* **2023**, *247*, 120693; f) Z. Han, X. Xiao, H. Qu, M. Hu, C. Au, A. Nashalian, X. Xiao, Y. Wang, L. Yang, F. Jia, T. Wang, Z. Ye, P. Servati, L. Huang, Z. Zhu, J. Tang, J. Chen, *ACS Appl. Mater. Interfaces* **2022**, *14*, 1850-1860.

[18] Z. Jiang, R. Dong, A. M. Evans, N. Biere, M. A. Ebrahim, S. Li, D. Anselmetti, W. R. Dichtel, A. G. Livingston, *Nature* **2022**, *609*, 58-64.

[19] M. Wang, S.-L. Li, Y. Chen, Q. Duan, D. Cheng, G. Gong, Y. Hu, *J. Membr. Sci.* **2024**, *698*, 122605.

[20] a) Y. Wen, R. Dai, X. Li, X. Zhang, X. Cao, Z. Wu, S. Lin, C. Y. Tang, Z. Wang, *Sci. Adv.* **2022**, *8*, eabm4149; b) Y. Wang, R.-Z. Liang, T.-Z. Jia, X.-L. Cao, Q. Wang, J.-R. Cao, S. Li, Q. Shi, L. Isaacs, S.-P. Sun, *J. Am. Chem. Soc.* **2022**, *144*, 6483–6492; c) K. Wang, X. Wang, B. Januszewski, Y. Liu, D. Li, R. Fu, M. Elimelech, X. Huang, *Chem. Soc. Rev.* **2022**, *51*, 672-719.

[21] S. Zhao, Z. Zhao, Z. Zha, Z. Jiang, Z. Wang, M. D. Guiver, *Adv. Funct. Mater.* **2024**, DOI: 10.1002/adfm.202314469.

[22] a) I. Vural Gürsel, T. Noël, Q. Wang, V. Hessel, *Green Chem.* **2015**, *17*, 2012-2026; b) J. Dreimann, P. Lutze, M. Zagajewski, A. Behr, A. Górak, A. J. Vorholt, *Chem. Eng. Process.* **2016**, *99*, 124-131.

[23] a) E. Yang, M. Kim, Y. Liang, J. Byun, H. Kim, J. Kim, H. Choi, *Chem. Eng. J.* **2023**, *474*, 145339; b) M.-B. Wu, F. Yang, J. Yang, Q. Zhong, V. Körstgen, P. Yang, P. Müller-Buschbaum, Z.-K. Xu, *Nano Lett.* **2020**, *20*, 8760–8767.